PAPER

Check for updates

Deciphering the mechanism of water interaction with nanostructural copper oxide: going beyond superwetting†

Julia Moszczyńska,[a] Xinying Liu, [iD] [b] Yali Yao[b] and Marek Wiśniewski [iD] *[a]

The interaction of water molecules with copper oxide nanowires (nW-CuO) was comprehensively studied. The obtained results prove that nW-CuO is a perfect material for water purification *via* photothermal conversion in solar interfacial evaporation. Measurements of the water contact angle (WCA) close to zero degrees lead to a conclusion about the superwetting state. However, in such a case, the questions appear: do we measure the neat surface properties? To what extent does the water film affect the surface properties? These problems were addressed by synthesizing nW-CuO(X), where X is the desorption temperature, and assessing the effect of H_2O pre-adsorption through air exposure using nW-CuO(25). The sample was characterized on a molecular level by Raman and far-infrared spectroscopy and XRD, proving the synthesis of the typical CuO material. Some meaningful differences in surface energy values between nW-CuO(200) and nW-CuO(25) were detected based on immersion enthalpy. These differences were proved to originate from a different concentration of surface Langmuir-type highly active adsorptive centers determined by the H_2O adsorption isotherm. The adsorption enthalpy measurement also reveals dissociative H_2O adsorption in the low-coverage region on nW-CuO(200). For both samples, the entropic factor plays a dominant role during adsorption under high humidity conditions. As a consequence of mobile adsorption, H_2O molecules retain partial freedom of movement, which reduces entropy loss and heat of evaporation to *ca.* -7 kJ mol^{-1}. Such a low value of the desorption enthalpy promotes efficient evaporation from the material surface with a rate of 3.02 kg m^{-2} h^{-1} under minimal temperature increase.

Introduction

Wettability is a crucial property of a material surface. It plays an essential role in surface chemistry and materials science.[1,2] From fuel cells and batteries,[3,4] through superwetting surfaces for catalysts,[5,6] to dealing with oily wastewater pollution,[7] materials with specially designed wettability have been widely used in industry and agriculture.[8,9] In recent years, the super-wettability of tested systems has attracted researchers' attention for solving problems in the areas of energy, health, and the environment.[10–13]

Considerable attention has been paid to investigating the synthesis, structures, properties, and applications of copper oxide nanostructures. One of the most important reasons is that CuO is a non-toxic and low-cost material. Moreover, it belongs to semiconductors with a narrow bandgap of 1.2 eV. The promising applications in numerous science and technology branches make these structures the subject of interest.[14,15] CuO is a widely utilized compound in environmental applications, demonstrating proven effectiveness in adsorbing chromium and arsenic from water, as well as in purifying organic contaminants.[16–18]

The basis of most CuO synthesis methods is the dehydration of copper hydroxocomplexes. It could be done in many different ways. The most popular are hydrothermal,[19,20] dry (air annealing),[21] and wet chemical methods.[22] By using these methods, different shapes of materials can be obtained. Among others, CuO nanoflowers were synthesized by Gu *et al.*[19] using the hydrothermal method. The nanoflower-, nanosheet-, and nanobundle-type structures that depended on the concentration of NH_3 in the solution were synthesized by Zhang *et al.*[19] The authors prepared nanostructures of CuO with a surfactant-assisted wet-chemical method followed by thermal treatment. The nanowire form of CuO nanostructures was

[a] *Department of Materials Chemistry Adsorption and Catalysis, Faculty of Chemistry, Nicolaus Copernicus University in Toruń, Gagarina 7, 87-100 Torun, Poland. E-mail: marekw@umk.pl*

[b] *Institute for Catalysis and Energy Solutions, University of South Africa, c/o Christiaan de Wet & Pioneer, Florida 1709, Roodepoort, Gauteng, South Africa*

† Electronic supplementary information (ESI) available. See DOI: https://doi.org/10.1039/d5ma00443h

obtained by Sundar *et al.*[23] Authors used the saponin-rich *Sapindus mukorossi* fruit extract during synthesis.

The electrochemical and photocatalytic properties are the most frequently investigated using nanostructured CuO. During these studies, water is the essential medium; thus, knowledge about CuO–H_2O interaction is crucial.

To our knowledge, only a few studies have raised the subject of water adsorption on a CuO surface. Azimirad *et al.*[20] described the synthesis of CuO nanopowders by hydrothermal treatment of copper salt solutions. Using copper nitrate resulted in nanorods, copper sulfate led to nanoplatelets, and copper acetate produced nanoflowers. The authors investigated water adsorption on the surface of these three types of nanostructures and correlated the results with their antibacterial activities against *Escherichia coli*. Among them, nanorods synthesized from copper nitrate demonstrated the highest antibacterial efficacy.

The synthesis of nanostructural CuO is the subject of several investigations, but very few of them take into account how the morphology and structure of the resulting particles impact their characteristics. On the other hand, nanostructural CuO was considered as a part of composite materials for Janus-type solar evaporators.[24] CuO is usually chosen because of its p-type semiconductor character with good photothermal properties.[25]

The superwetting state of CuO has been investigated recently by Wu *et al.*[26] It was shown that CuO nanotip-arrays possess extraordinary superwetting properties with an ultra-short wetting time for water. The convex hierarchical structure explains observed phenomena and a superior water affinity to CuO.[26,27]

To the author's knowledge, there is no literature linking the differentiation of superwetting properties of materials with the photothermal properties of the tested materials based on comprehensive studies of the interactions between the CuO surface and water. In the present work, we would like to take a step further and attempt to identify certain critical factors distinguishing the apparently similar properties, *i.e.*, close to zero-water contact angle (WCA). The degree of water ordering influences both the surface energy and the interfacial characteristics of the wetted material. The water layer formed at the surface of metal oxides can modify the wetting angle and increase the hydrophilicity of the material. This leads to an apparent hydrophilicity, where the water layer effectively conceals the intrinsic hydrophobic nature of the surface.[28,29] The main goal of this work is to demonstrate how the water film that forms on nanowire surfaces affects the interactions between CuO and water. This investigation seeks to explain how the properties of nanomaterials are influenced by both pre-adsorption and nanometric size. In addition, the study explores a more cost-effective method for synthesizing nanostructured CuO in the form of nanowires. The most unique aspect of this research is the link between superwetting and photothermal properties. A thorough thermodynamic analysis enabled a precise description of the adsorbent–adsorbate interactions, which is an insight not previously provided in the existing literature.

Experimental

Materials and methods

General procedure for synthesis. 25 mL of saturated $Cu(NO_3)_2$ solution was added to 100 mL of 6 mol L^{-1} NaOH and stirred magnetically for 30 min. 20 mL of concentrated H_2SO_4 acid was added to this slurry to generate nW-CuO. Brown precipitates that appeared were rinsed with water and repeatedly decanted several times until the characteristic reactions to SO_4^{2-} vanished. Finally, the samples were lyophilized (10 Pa, -40 °C). Before each experiment, samples were outgassed at 25 or 200 °C and labeled as nW-CuO(25) or nW-CuO(200), respectively.

Characterization and analysis methods

Raman measurements. The nonpolarized spectra of CuO nanostructures were investigated in the spectral range of 60–4500 cm^{-1}. Raman spectra were recorded in the backscattering geometry using the SENTERRA micro-Raman system. We used a green laser operating at 532 nm as an excitation light. The laser beam was tightly focused on the sample surface through a 30× microscope objective. To prevent any damage of the sample, an excitation power was fixed at 2 mW. A resolution of 4 cm^{-1}, CCD temperature of 223 K, laser spot of about 10 μm, and a total integration time of 100 s (50 × 2 s) were used. The position of the microscope objective with respect to the sample was piezoelectrically controlled (XY position).

XRD measurements. Bulk samples were characterized by PXRD using Philips XPERT Pro θ–2θ and Bruker D8 diffractometers with CuKα1 and CuKα radiation, respectively. Data were collected over the range $5 \leq 2\theta/° \leq 120$, with a step size of $0.0084°$ 2θ and a scanning rate of $0.02°$ min^{-1}.

Scanning electron microscopy (SEM) studies. Scanning electron microscopy (SEM) studies were performed with a Quanta 3D FEG (EHT = 30 kV) instrument. Samples were placed onto carbon tabs attached to aluminum SEM stubs. All samples were analyzed in the microscope without coating treatment.

FTIR spectroscopy data. FTIR spectroscopy data were acquired by using a Vertex V70 (Bruker Optic), in ATR mode techniques (single reflection using diamond crystal), or in the transmission mode for TPD experiments in the frequency range of 6000–15 cm^{-1}.

For transmission mode, the sample loaded on the Si-wafer was dried at 25 °C under a vacuum. After the equilibrium was reached, the temperature was raised up to 200 °C with the ramp at 5 °C min^{-1}.

Calorimetric analysis. Water vapor adsorption isotherms were measured volumetrically at 298 K, and differential enthalpy of adsorption (q^{diff}) was determined using a Tian–Calvet isothermal microcalorimeter constructed in our laboratory.[30] The related molar entropy changes of the adsorbed molecules (ΔS) were calculated using the basic thermodynamic relations (eqn (S1), ESI†).

Adsorption kinetics. To describe H_2O adsorption kinetics, where the rate-determining step is the existence of a barrier to diffusion, a stretched exponential (SE) model, which is

described by eqn (S4) (ESI†), was used. Note that β is the exponential parameter of the adsorption process.[31,32]

Photothermal activity studies

The photothermal conversion properties of nW-CuO(X) with different concentrations (0 to 0.02 wt%) were recorded using a self-built photothermal conversion device (805 nm 50 W LED lamp) with an output flux set at 0.9 W cm^{-2}. The temperature of the samples' solutions was monitored continuously *via* a thermocouple sensor.

During the irradiation, the real-time mass changes of the evaporator were recorded. An expandable polyethylene vessel was used to provide an adiabatic environment.

Results and discussion

Due to, *e.g.*, acid addition to the (hydroxo)–copper(II) complex solution, CuO precipitation occurs *via* the dehydration process. The addition of different acids leads to the formation of varied nanostructures. The addition of concentrated H_2SO_4 leads to the formation of nanowires. Interestingly, almost all nanowires are *ca.* 10 μm long with a diameter of *ca.* 25 nm (Fig. 1a and Fig. S1, ESI†). The measured WCA is close to zero (Fig. 1b). Such observed superwetting properties of the material perfectly agree with the literature data.[23,24]

Performed spectroscopic investigations (see Fig. 1c–e) proved that the material has a typical CuO nanostructure at the molecular level, identical to the literature data.[33]

The CuO monoclinic phase is generally associated with the C_{2h}^{6} space group, possesses three acoustical modes ($A_u + 2B_u$), six IR-active modes ($3A_u + 3B_u$), and three Raman-active modes

($A_g + 2B_g$). The A_g mode appears at 287 cm^{-1}, whereas the B_g modes are responsible for the peaks at 332 and 620 cm^{-1}.

X-ray diffraction is a method that allows to determine the purity and crystallinity of samples.[29,34,35] The results obtained from XRD confirm the high purity of the received nanomaterials (Fig. 1e). The main peaks at 35.7° and 38.9° correspond to the (002) and (111) crystal planes of CuO (JCPDS no. 89-5899). Low intensities of those signals confirm that nanostructural CuO formation occurred during liquid-phase synthesis. Moreover, the calculated average crystalline size based on the Scherrer formula is 23.3 and 22.4 nm, respectively, for the (002) and (111) planes. The values are highly consistent with the corresponding SEM images of the CuO nanocrystals.

Strong H_2O interaction with the nW-CuO(X) surface was demonstrated by a series of experiments, which also examined the impact of water film formation upon exposure to water vapor in the air.

The low-temperature N_2 adsorption isotherms are type II for both samples (nW-CuO(200) and nW-CuO(25)) with small hysteresis type H3 (Fig. 2a). Besides similarities in adsorption mechanisms, the tested samples differ in the pore volume and specific surface area: 69 and 48 m^2 g^{-1} based on the BET model, and 45 and 30 m^2 g^{-1} based on the DFT model, for nW-CuO(200) and nW-CuO(25), respectively. The differences in pore size and surface area distribution indicate that some centers are inaccessible for N_2, while H_2O was preadsorbed on the surface. Nevertheless, the determined values of specific surface areas and isotherm types are comparable to those reported in the literature for CuO nanostructures.[36–38]

In situ FTIR studies were then performed. Strong mutually overlapped bands in the $v(OH)$ region evidence a high amount
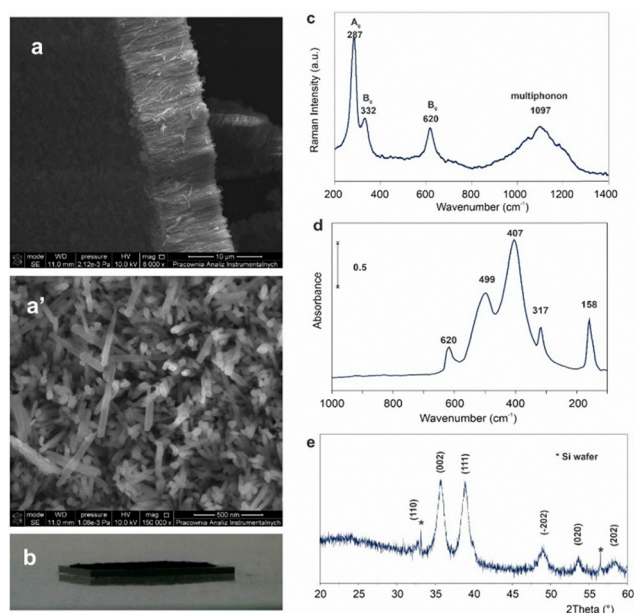

Fig. 1 (a) and (a′): SEM pictures of synthesized nanowires nW–CuO, and its (b): water contact angle (WCA) equal to zero. Structural characterization: (c): Raman; (d): far IR; (e): XRD (note that only the FIR sample was vacuum treated at 200 °C).
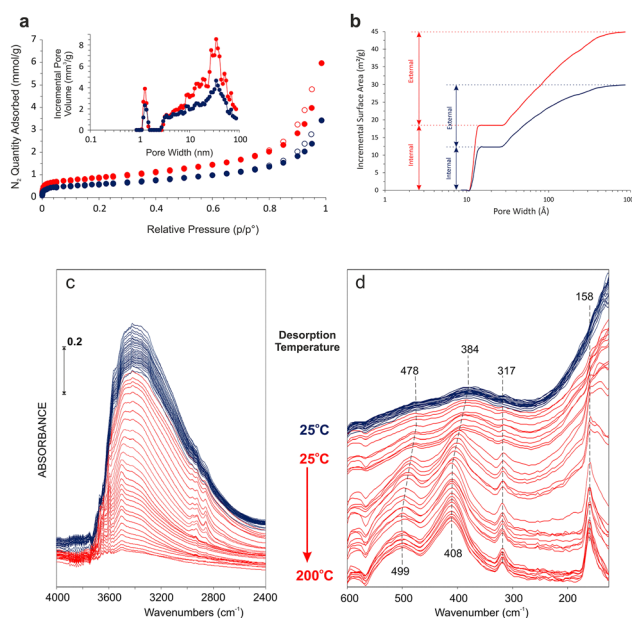

Fig. 2 (a) Low-temperature N_2 adsorption (inset: pore size distribution), (b): cumulative surface area distribution, (c) and (d): the FTIR spectra registered during the temperature-programmed desorption (note that blue and red colors are for nW–CuO(25) and nW–CuO(200), respectively).

of adsorbed water (Fig. 2c). Moreover, the water layer completely shields the CuO bands in the FIR region (Fig. 2d). To the best of our knowledge, this effect is unreported in the existing literature.

It is noteworthy that only a small portion of the adsorbed H_2O is removed by desorption at 25 °C. The temperature must be raised over 200 °C to completely eliminate the water coating. An additional effect proving the strong interaction of H_2O with the CuO surface is due to the analysis of spectral changes during temperature-programmed desorption in the far IR region, shown as bands blue-shifting when water is removed from the structure (Fig. 2d). At a low-temperature regime, *i.e.*, below 50 °C, adsorbed water molecules cause weakening (and extension) of Cu–O bonds observed as the red-shift of the 499 and 408 cm^{-1} signals.

Assuming CuO bulk density equals 6.31 g mL^{-1}, one can calculate the geometric surface area of *ca.* 26 m^2 g^{-1}. The value is perfectly matched with the external area determined from DFT calculations (Fig. 2b). The decrease in surface areas after H_2O pre-adsorption is related to filling all the roughness present on the nW-CuO surface and space between the nanowires (the secondary pore structure). The latter can be assumed due to similarities to CNTs.[39–41]

Fig. 3 shows the photothermal conversion curves of the pure CuO dispersed in water with different concentrations. In each experiment, the starting temperature was *ca.* 20 °C. The subsequent temperature data were collected with intervals of 60 s. As can be seen, the temperatures of all solutions rise continuously under the irradiation. The heating rate increases with the increase in concentration. After a certain period of time, the temperatures of all the nanofluids reach their maximum and remain stable. The maximal temperature appears at the highest concentration of 0.02 wt%, of about 36.6 °C, corresponding to a temperature difference (ΔT) of about 16.6 °C.

The presented results indicate that the concentration of the solutions has a great influence on the maximum temperatures, although they do not belong to the maximum ones described in the literature.[42,43] Nevertheless, with such a small ΔT, the evaporation rate of the level of 3.02 kg m^{-2} h^{-1} at 0.5 sun is surprising.

The causes of the observed phenomena should be sought both in the values of surface energies and H_2O adsorption parameters. The results presented in Fig. 1 prove that nW-CuO(25) is already superwetting based on WCA measurement;

Table 1 The thermodynamic parameters collection: enthalpies of immersion (h_i, i = water, *n*-heptane, formamide, and nitropropane), the surface energy (H_S^T) components (acidic H_S^+ and basic H_S^-), the work of adhesion, W_{adh}, and the surface electrostatic field strength (F) of nW-CuO(200) and nW-CuO(25) to water. The values of the surface energy components of the different probe liquids used in this study are from the literature[47]

	nW-CuO(200)	nW-CuO(25)
h_{water} [mJ m^{-2}]	−197.1 (8.5)	−89.7 (4.6)
$h_{n\text{-heptane}}$ [mJ m^{-2}]	−214.5 (13.4)	−212.1 (11.3)
$h_{formamide}$ [mJ m^{-2}]	−380.1 (18.8)	−191.8 (9.4)
$H_{nitropropane}$ [mJ m^{-2}]	−373.2 (21.2)	−214.9 (14.5)
H_S^{LW} [mJ m^{-2}]	356.9 (24.3)	350.6 (26.4)
H_S^+ [mJ m^{-2}]	189.8 (16.9)	0.02 (0.004)
H_S^- [mJ m^{-2}]	47.3 (3.3)	1.9 (0.22)
H_S^T [mJ m^{-2}]	451.7 (28.1)	350.6 (18.9)
W_{adh} [mJ m^{-2}]	491.2 (43.8)	242.8 (14.3)
F [MV m^{-1}]	2662 (122)	48 (2.1)

thus, another technique should be used. The simplest solution is to measure the enthalpies of immersion in different probe liquids to characterize the surface energy components using the van Oss–Good–Chaudhury (VGC) approximation. The model easily separates the Lifshitz–van der Waals component of the surface energy, H_S^{LW}, from the acidic, H_S^+, and the basic, H_S^-, factors, allowing calculation of the total surface energy, H_S^T.[44] In order to achieve the H_S^T, the enthalpies of immersion in different probe liquids, *viz.* water, *n*-heptane, and formamide (h_i), were measured, and the results are collected in Table 1. The results show that nW-CuO(200) possesses somewhat more acidic than alkaline properties, and its extremely high water work of adhesion value proves the superwetting ability of the material.

The vacuum treatment at only 25 °C (nW-CuO(25)), as one could expect, does not influence the dispersive component (H_S^{LW}). In contrast, the electrostatic terms (H_S^+ and H_S^-) decrease close to zero. As a consequence, W_{adh} decreases significantly, too, thus promising to change the adsorption mechanism.

Based on the above, we need to look closer at water adsorption on nW-CuO. When water is adsorbed on highly hydrophilic surfaces, the D'Arcy and Watt (DW) adsorption isotherm model (Fig. 3a, b and eqn (S2), ESI†) should be considered.[45,46] This simple approximation assumes that water adsorption occurs quite independently on stronger, high-energy, and on weaker, low-energy sites.

The former primary binding centers ($a_{mL,2}$) mainly consist of superhydrophilic groups. Their calculated values exceed 13.5 μmol m^{-2} for both samples (Table 2).

The corresponding values of the Langmuir constant (K_L), which is the parameter defining the energy of the process, equal *ca.* 3.8 and are responsible for the occurrence of the "knee-shape" of the isotherms in the low-pressure range below $p/p_s = 0.005$. Further increase in H_2O pressure reveals the type-II adsorption isotherm, which is also suitable for fitting with the DW model. The value of parameter c – defined as the ratio of adsorption and desorption constants of *ca.* 0.94 suggests the presence of highly interacting sites.
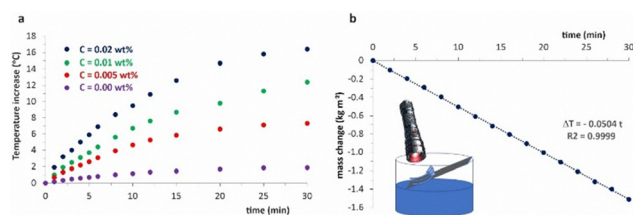

Fig. 3 (a) Temperature changes of the solutions under irradiation with an 805 nm laser (0.8 W cm^{-2}) and (b) the corresponding solar-to-vapor generation efficiency during evaporation under an equivalent of 0.5 sun.

Table 2 The estimated parameters of the DW model for water adsorption on nW–CuO(200) and nW–CuO(25)

Sample	nW–CuO(200)	nW–CuO(25)
$a_{mL,1}$ [μmol m^{-2}]	4.362	0.00
$K_{L,1}$	398.1	—
$a_{mL,2}$ [μmol m^{-2}]	13.68	13.54
$K_{L,2}$	3.769	3.841
C	0.942	0.936
a_0 [μmol m^{-2}]	6.67	11.04
R^2	0.9987	0.9977

When water is removed from the nW-CuO surface, one needs to assume an additional term as the primary center on nW-CuO(200) (Fig. 4a). The presence of 4.36 μmol m^{-2} with tremendous values of the Langmuir constant (K_L = 398) was calculated. Notably, these primary centers originate from secondary sites (a_0) and are responsible for the presence of highly acidic and basic sites.

Measured in parallel, the differential adsorption enthalpy (ΔH) enabled calculating the thermodynamic functions. Gibbs free energy for both samples is negative in the whole pressure range (Fig. 4a′ and b′). Its values are more negative for low p/p_s regimes as a consequence of very high adsorbate–adsorbent interactions.

Conversely to what was expected, the measured differential heat of adsorption values in the low-pressure range are close to zero, especially for nW-CuO(200) (Fig. 4a′). Zeroing the q^{diff} values seems unusual, considering the number of high-energy

sites. To explain this phenomenon, one must consider that the total effect is observed during calorimetric studies. The algebraic sums of energetically opposed processes are measured. The first natural candidate is CuO bond stretching, observed as red-shifting in Fig. 2. The other is H_2O dissociative adsorption on highly acidic and basic sites (Table 1). It is worth noting that this step is absent for the nW-CuO(25) sample (Fig. 4b).

The increase in relative H_2O pressure causes typical behavior, *i.e.*, adsorption in this region is enthalpy-dependent, where a monolayer ($a_{mL,2}$) can be formed. Also, the entropy of the process decreases due to the increase in order in the adsorption layer (Fig. 4b′).

Further increase in the relative pressure p/p_s above the value of 0.5 is accompanied by unexpected effects: a decrease in the absolute value of ΔH and positive values of the entropic factor ($T\Delta S$). This is observable for both samples and is explained by mobile adsorption (*e.g.* 2D gas on the surface), where the molecules retain partial freedom of movement while limiting entropy loss.

The assumptions explain the existence and separation of two signals (endo- and exothermal) shown in Fig. S2 (ESI†), clearly observed at the low-pressure range on nW-CuO(25), where ΔG depends on the enthalpy, and where the entropy change during adsorption is negative ($T\Delta S < 0$). Such a decrease is due to the reduction in randomness due to the formation of H_2O clusters (Fig. 5).

The positive values of the entropic term of ΔG are also observed in higher relative pressure ranges for both measured
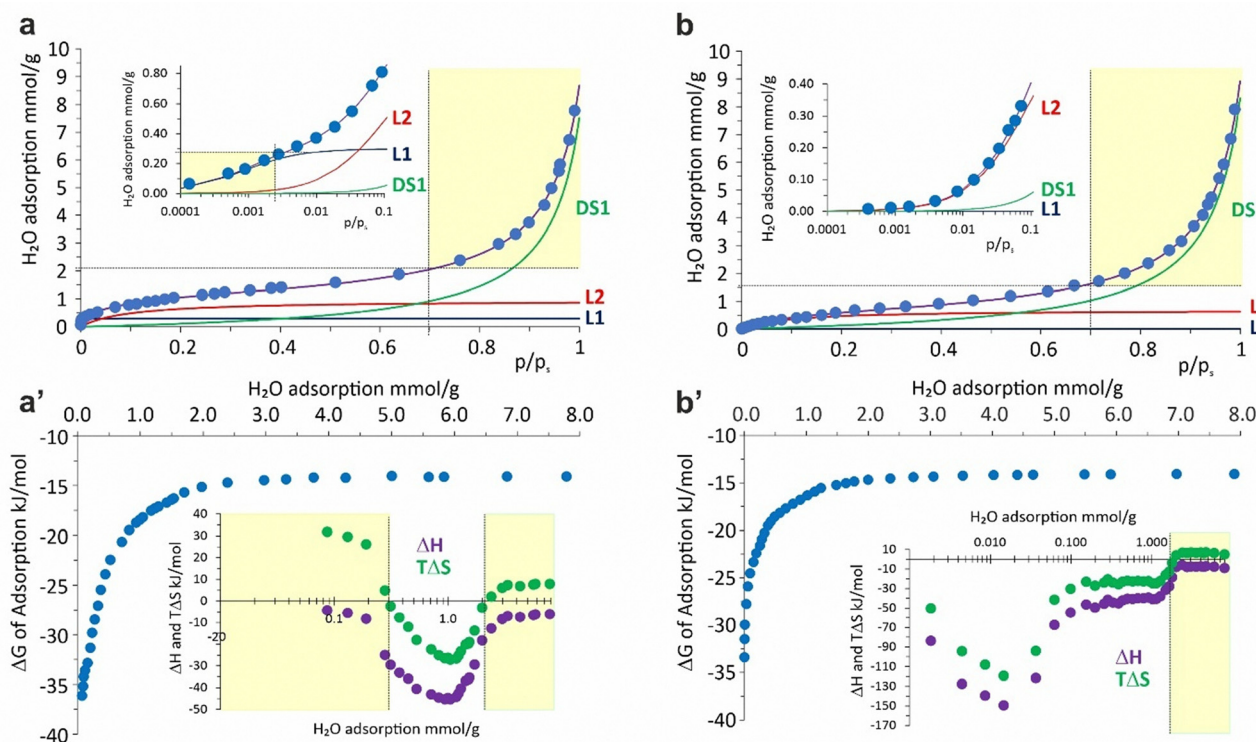

Fig. 4 Water adsorption isotherm on (a): nW-CuO(200) (b): nW-CuO(25). Marked areas are for entropy-derived Gibbs free energy changes, which are shown in (a′) and (b′); note that insets in (a′) and (b′) show changes in the values of the components of the ΔG.
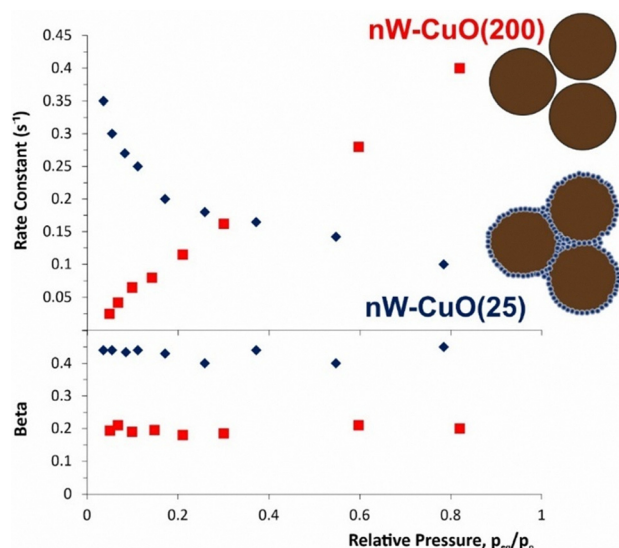
Fig. 5 Changes in the rate constant and β-parameter during H_2O adsorption on nW-CuO(200) – red and nW-CuO(25) – blue.

samples. Note that the presence of these areas confirms the accuracy of the DA model – *i.e.*, the separation of primary and secondary sites where an association between single adsorbate molecules and adsorbent occurs.

Adsorption is typically characterized as an exothermic process that causes an enthalpy reaction. Instances of entropy-driven adsorption have been reported, particularly in cases involving large polymer chains or hydrogen spillover. The observed

entropy dominance may be attributed to factors such as the release of structured interfacial water, increased configurational flexibility, or surface reorganization. These findings further underscore the significant influence of nanostructure on thermodynamic behavior.[48–50]

According to the results shown in Fig. 4a and b, at low pressure (low surface coverage), H_2O adsorption occurs mainly by hydrogen bonding to primary surface centers. The adsorption kinetics is influenced by two main factors: (a) the strength of the interaction with the surface functional groups and (b) the barriers to diffusion into the secondary pore structure. Strong interaction causes a high barrier, so the H_2O adsorption for nW-CuO(200) is slower than for nW-CuO(25). This is consistent with a distribution of primary centers (Tables 1, 2 and Fig. 4a, b) and reflects surface heterogeneity.

At a high relative pressure regime, the availability of surface groups decreases with increasing adsorption, and the adsorbate-adsorbate interactions in the associative mechanism become increasingly significant. When the value of p/p_o exceeds 0.3, the higher barriers to the diffusion of H_2O into nW-CuO(25) as compared to dry, *i.e.*, dehydrated surfaces, imply more marked kinetic differences for H_2O adsorption.

The stretched exponential (SE) model, which is described by eqn (S4) (ESI†), was used successfully to describe the adsorption of H_2O on tested samples (see also Fig. S4, ESI†). The exponent β covers the range $0 < \beta < 1$ and represents a hierarchy of waiting times for defects hopping in a random environment.[51] Thus, the SE model can describe one-dimensional
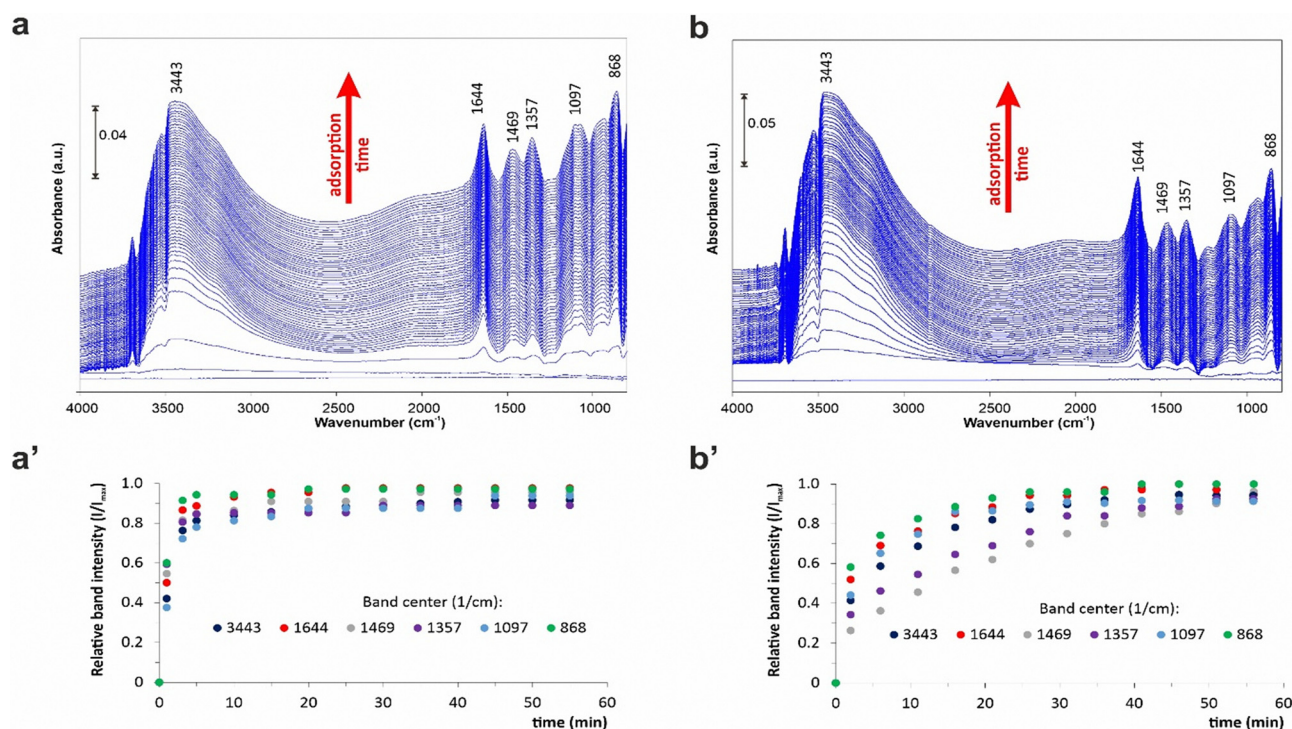

Fig. 6 Spectral changes induced by H_2O adsorption on (a) nW-CuO(200) and (b) nW-CuO(25). The bottom panels (a′) and (b′) collect the quantitative data (note that $p/p_s = 0.9$, in Ar with a total flow rate of 50 mL min^{-1} was used).

phenomena with a distribution of relaxation times when β is 0.5, and three-dimensional (3D) phenomena with a single relaxation time when $\beta = 1$.

Calculated in our case, values of β as low as 0.2 for nW-CuO(200) and 0.4 for nW-CuO(25) suggest that the curvature of nanowires and secondary pore-structure may be of decisive importance and describe one-dimensional processes. Interestingly, when considering very low values of rate constants for the sample without the water film, β being far below 0.5 should describe the 0D-point adsorption process. This confirms positive values in the $T\Delta S$ term, endoenergetic effects during adsorption, the presence of L1 active centers, and very high acid/base components of surface energy.

We employed the *in situ* measurements to look for the mechanism of the process of H_2O adsorption on the CuO surface, and the results are presented in Fig. 6 and Fig. S5 (ESI†).

In the experiment, the background was the sample spectrum registered just before the material was exposed to water. Therefore, in addition to positive ones, it is possible to observe negative signals, indicating the disappearance of a given surface structure.

The adsorption of H_2O is accompanied by the appearance of a number of surface structures on both materials visible as IR bands at 3443, 1644, 1469, 1357, 1097, and 868 cm^{-1}. The first two of these are typical water bands responsible for the stretching and bending vibrations of the –OH groups. The kinetics of their formation and disappearance during desorption (Fig. S5, ESI†) are equal, confirming the bands' assignment to the same structures. The slight differences are due to the complexity of the –OH stretching vibration band. The main reasons for the differences are the hydroxyl groups present in the starting material and the hydrogen bonds.

Very interesting are the remaining signals. The couple of 1469 and 1357 cm^{-1} in the literature are interpreted as surface carbonate structures.[52,53] The results presented in this paper contradict such assumptions. There are several pieces of evidence: first, in *in situ* experiments, the sample comes into contact only with ultra-pure carrier gas (Ar), we use deionized water purged all the time *via* Ar, and finally, for comparison, we measured the spectra of nW-CuO(200) after CO_2 adsorption – the results presented in Fig. S6 (ESI†) are unambiguous – the signals at 1469, 1357 cm^{-1} should not be attributed to carbonate structures.

Moreover, considering their removal from the CuO surface is slow (see Fig. S6, ESI†) and the chemical nature of the material surface (Table 1), the bands at 1469, 1357 and 1097 cm^{-1} should be attributed to surface structures containing hydrated Eigen–Zundel type protons.[54,55] However, additional studies are required to confirm this hypothesis.

Finally, the kinetic studies prove that the band with a maximum at 868 cm^{-1} cannot be interpreted as a wagging vibration of adsorbed H_2O molecules due to the different desorption rates (Fig. S5, ESI†). Bearing in mind its low stability, we suggest that surface peroxide species are responsible for this signal's presence.

Conclusions

Solar interfacial evaporation is an effective strategy for addressing water scarcity. However, its efficiency is often hindered by factors such as high enthalpy requirements for steam generation. The findings of this study suggest that nanostructured CuO, owing to its unique properties, enhances evaporation efficiency by reducing the energy barriers associated with water adsorption and desorption. The consequences of superwetting properties in combination with a lowering of work adhesion when a water film is formed on the surface of nanostructural CuO are unusual photothermal properties. Low adsorption/desorption enthalpy values and the formation of the mobile phase on the nW-CuO surface enable efficient H_2O desorption from the surface. The full knowledge of the adsorbent surface properties leads to an exceptional water purification rate of 3.02 kg m^{-2} h^{-1}. This combination of high photothermal conversion and low desorption enthalpy strategies opens a bright future for processes solving water scarcity problems. While these studies demonstrate significant implementation potential, they were conducted at the laboratory scale. Consequently, large-scale field tests for desalination are necessary to validate their practical applicability. Given its numerous advantages, CuO emerges as a promising candidate for such applications. Nonetheless, it is advisable to expand the research to include other oxide and nanostructured materials to explore broader possibilities.

Author contributions

Conceptualization: MW and JM; methodology: MW and JM; validation: JM, XL., and YY.; investigation: MW, JM, YY, and XL; data curation: JM, MW, and YY; original draft preparation: MW, JM, and XL; review & editing: MW, YY, and XL; visualization: MW and XL; supervision: YY.

Conflicts of interest

There are no conflicts to declare.

Data availability

The datasets obtained during the current study are available from the corresponding authors on reasonable request.

Acknowledgements

References

1 T. Sun, L. Feng, X. Gao and L. Jiang, *Acc. Chem. Res.*, 2005, **38**, 644.

2 M. Liu, S. Wang, Z. Wei, Y. Song and L. Jiang, *Adv. Mater.*, 2009, **21**, 665.

3 J. B. Habedank, F. J. Günter, N. Billot, R. Gilles, T. Neuwirth, G. Reinhart and M. F. Zaeh, *Int. J. Adv. Des. Manuf. Technol.*, 2019, **102**, 2769.

4 D. H. Jeon, *Energy Storage Mater.*, 2019, **18**, 139.

5 H. M. Chen, C. K. Chen, R. S. Liu, L. Zhang, J. Zhang and D. P. Wilkinson, *Chem. Soc. Rev.*, 2012, **41**, 5654.

6 C. Meng, B. Wang, Z. Gao, Z. Liu, Q. Zhang and J. Zhai, *Sci. Rep.*, 2017, **7**, 1.

7 A. Samanta, Q. Wang, S. K. Shaw and H. Ding, *Mater. Des.*, 2020, **192**, 108744.

8 K. Liu and L. Jiang, *Nanoscale*, 2011, **3**, 825.

9 W. Zhang, Z. Shi, F. Zhang, X. Liu, J. Jin and L. Jiang, *Adv. Mater.*, 2013, **25**, 2071.

10 T. Kong, G. Luo, Y. Zhao and Z. Liu, *Adv. Funct. Mater.*, 2019, **29**, 1808012.

11 B. Su, Y. Tian and L. Jiang, *J. Am. Chem. Soc.*, 2016, **138**, 1727.

12 M. Liu, S. Wang and L. Jiang, *Nat. Rev. Mater.*, 2017, **2**, 17306.

13 Y. Wu, J. Feng, H. Gao, X. Feng and L. Jiang, *Adv. Mater.*, 2019, **31**, 1800718.

14 B. Heng, C. Qing, D. Sun, B. Wang, H. Wang and Y. Tang, *RSC Adv.*, 2013, **3**, 15719.

15 M. Dorogov, A. Kalmykov, L. Sorokin, A. Kozlov, A. Myasoedov, D. Kirilenko, N. Chirkunova, A. Priezzheva, A. Romanov and E. C. Aifantis, *Mater. Sci. Technol.*, 2018, **34**, 2126.

16 E. M. N. Polman, G.-J. M. Gruter, J. R. Parsons and A. Tietema, *J. Polym. Environ.*, 2020, **28**, 47–60.

17 K. Z. Elwakeel and E. Guibal, *Carbohydr. Polym.*, 2015, **134**, 190–204.

18 W. Xie, Z. Wang, Y. Yin, Y. Bai, J. Yang, D. Miao, X. Zeng, S. Yang and G. Wang, *Water Res.*, 2025, **284**, 124023.

19 A. Gu, G. Wang, X. Zhang and B. Fang, *Bull. Mater. Sci.*, 2010, **33**, 17.

20 R. Azimirad, S. Safa and O. Akhavan, *Acta Phys. Pol., A*, 2015, **127**, 1727.

21 K. Zhang, C. Rossi, C. Tenailleau, P. Alphonse and J. Chane-Ching, *Nanotechnology*, 2007, **18**, 275607.

22 Y. X. Zhang, M. Huang, F. Li and Z. Quan Wen, *Int. J. Electrochem. Sci.*, 2013, **8**, 8645.

23 S. Sundar, G. Venkatachalam and S. J. Kwon, *Nanomaterials*, 2018, **8**, 823.

24 L. Hou, N. Wang, L.-J. Yu, J. Liu, S. Zhang, Z. Cui, S. Li, H. Li, X. Liu, L. Jiang and Y. Zhao, *ACS Energy Lett.*, 2023, **8**, 553.

25 Q. Zhang, K. Zhang, D. Xu, G. Yang, H. Huang, F. Nie, C. Liu and S. Yang, *Prog. Mater. Sci.*, 2014, **60**, 208.

26 Y. Wu, S. Wang, S. Ju, Z. Zhou, T. Wang, T. Hang and M. Li, *ACS Appl. Nano Mater.*, 2021, **4**, 4713.

27 F. M. Chang, S. L. Cheng, S. J. Hong, Y. J. Sheng and H. K. Tsao, *Appl. Phys. Lett.*, 2010, **96**, 114101.

28 H. Xiong, D. Devegowda and L. Huang, *Langmuir*, 2020, **36**, 723–733.

29 P. Ma, Y. Liu and K. Han, *et al.*, *Friction*, 2024, **12**, 591–605.

30 M. Wiśniewski, G. Rychlicki and A. Arcimowicz, *Chem. Phys. Lett.*, 2010, **485**, 331.

31 H. K. Chagger, F. E. Ndaji, M. L. Sykes and K. M. Thomas, *Carbon*, 1995, **33**, 1405.

32 C. R. Reid and K. M. Thomas, *Phys. Chem. B*, 2001, **105**, 10619.

33 T. Yu, X. Zhao, Z. X. Shen, Y. H. Wu and W. H. Su, *J. Cryst. Growth*, 2004, **268**, 590.

34 M. Cai, Y. Liu, K. Dong, X. Chen and S. Li, *Chin. J. Catal.*, 2023, **52**, 239–251.

35 S. Li, M. Cai and C. Wang, *et al.*, *Adv. Fiber Mater.*, 2023, **5**, 994–1007.

36 S.-D. Seo, Y.-H. Jin, S.-H. Lee, H.-W. Shim and D.-W. Kim, *Nanoscale Res. Lett.*, 2011, **6**, 397.

37 L. Xu, Y. Xu, F. Wang, J. Zhang, Z. Wang, W. Zhao and W. C. Oh, *J. Korean Ceram. Soc.*, 2012, **49**, 151.

38 R. Chowdhury, A. Khan and M. H. Rashid, *RSC Adv.*, 2020, **10**, 14374.

39 M. Wiśniewski, P. A. Gauden, A. P. Terzyk, P. Kowalczyk, A. Pacholczyk and S. Furmaniak, *J. Colloid Interface Sci.*, 2013, **391**, 74.

40 P. A. Gauden, A. P. Terzyk, S. Furmaniak, M. Wiśniewski, P. Kowalczyk, A. Bielicka and W. Zieliński, *Adsorption*, 2013, **19**, 785.

41 S. Furmaniak, A. P. Terzyk, P. A. Gauden, P. J. F. Harris, M. Wiśniewski and P. Kowalczyk, *Adsorption*, 2010, **16**, 197.

42 J. Zheng, F. Wu, D. Yu and W. Wang, *Sep. Purif. Technol.*, 2025, **362**, 131864.

43 Y. Wang, Q. Qi, J. Fan, W. Wang and D. Yu, *Sep. Purif. Technol.*, 2021, **254**, 117615.

44 J. Taguta, B. McFadzean and C. O'Connor, *Miner. Eng.*, 2019, **143**, 105954.

45 R. L. D'Arcy and I. C. Watt, *Trans. Faraday Soc.*, 1970, **66**, 1236.

46 S. Furmaniak, P. A. Gauden, A. P. Terzyk and G. Rychlicki, *Adv. Colloid Interface Sci.*, 2008, **137**, 82.

47 J. M. Douillard, F. Salles, M. Henry, H. Malandrini and F. Clauss, *J. Colloid Interface Sci.*, 2007, **305**, 352.

48 S. Kang, X. Zhang, U. Shakeel, J. Guo, W. Zhu, I. S. Makarov, M. R. Khan, H. Xiao and J. Song, *Int. J. Biol. Macromol.*, 2025, **143402**.

49 A. Mahdavi-Shakib, T. N. Whittaker and T. Y. Yun, *et al.*, *Nat. Catal.*, 2023, **6**, 710–719.

50 R. Torrence Martin, *Clays Clay Miner.*, 1959, **8**, 102–114.

51 M. F. Shlesinger and E. W. Montroll, *Proc. Natl. Acad. Sci. U. S. A.*, 1984, **81**, 1280.

52 S. Lakkaboyana, K. Soontarapa, N. Asmel, V. Kumar, R. Kumar Marella, A. Yuzir and W. Yaacob, *Sci. Rep.*, 2021, **11**, 5686.

53 K. Coenen, F. Gallucci, B. Mezari, E. Hensen and M. van Sint Annaland, *J. CO$_2$ Util.*, 2018, **24**, 228.

54 S. Das, S. Imoto, S. Sun, Y. Nagata, E. H. G. Backus and M. Bonn, *J. Am. Chem. Soc.*, 2020, **142**, 945.

55 M. Wiśniewski, *Int. J. Mol. Sci.*, 2022, **23**, 14292.